Materials & Design 244 (2024) 113170

Contents lists available at ScienceDirect

Materials & Design

journal homepage: www.elsevier.com/locate/matdes

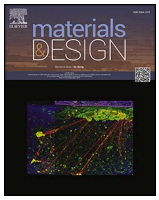

Investigation on the fatigue strength of AlSi10Mg fabricated by PBF-LB/M and subjected to low temperature heat treatments

Ilaria Roveda [a], Itziar Serrano-Munoz [a,*], Jan Haubrich [b], Guillermo Requena [b,c], Mauro Madia [a,**]

[a] Bundesanstalt für Materialforschung und –prüfung (BAM), Unter den Eichen 87, 12205 Berlin, Germany
[b] Institute of Materials Research, German Aerospace Center (DLR), Linder Höhe, 51147 Cologne, Germany
[c] Metallic Structures and Materials Systems for Aerospace Engineering, RWTH Aachen University, 52062 Aachen, Germany

ARTICLE INFO

Keywords:
PBF-LB/M AlSi10Mg
Fatigue strength
Defects
Kitagawa-Takahashi Diagram
Short Crack Models

ABSTRACT

This work provides an investigation of the influence of low temperature heat treatments on the fatigue behavior of a PBF-LB AlSi10Mg alloy. Fatigue specimens are produced in form of round bars on a build platform preheated at 200 °C. The specimens have been tested in three different conditions: as-built, and after heat treatments at 265 °C for 1 h and 300 °C for 2 h. Prior to the fatigue testing, the defect distribution is analyzed by means of micro computed tomography. Subsequently, the peak over threshold method is successfully applied to provide a prediction of the size of killer defect. The defect population was of gas porosity type. No clear improvement of the fatigue performance is observed after the heat treatments. The fatigue strength predicted using fracture mechanics-based approaches is in good agreement with the experimental data. Among the studied approaches, short crack models provided the most conservative predictions.

1. Introduction

Laser Powder Bed Fusion (PBF-LB/M) is an additive manufacturing (AM) technique that has gathered enormous amount of momentum thanks to its unprecedented possibilities of topology optimization and reduction of material waste [1,2]. Al-Si-Mg alloys, such as AlSi10Mg, have found extensive application in PBF-LB/M due to their good weldability, favorable mechanical properties, high heat conductivity, lightweight, corrosion resistance, and ductility improvement through heat treatment [3,4]. While the quasi-static mechanical properties of AM metallic components have been extensively studied and optimized, fatigue design and assessment remain significant challenges [5–8]. The inherent features of AM materials, such as microstructure inhomogeneity, defects, surface roughness, and residual stresses contribute to the complexity of assessing their fatigue behavior.

The as-built microstructure has received a lot of attention because it imparts a yield strength comparable to what can be achieved using the conventional T6 scheme ($\sigma_y > 200$ MPa). Moreover, the 3D network of fine α-Al cells surrounded by eutectic silicon promote a cage-effect that limits the accumulation of damage, for the case of a defect-free material [9]. Numerous studies have reported in the last years that manufacturing defects, including surface roughness in case of as-built surfaces, are the main factor influencing the fatigue performance of AMed metallic materials [10,11]. Furthermore, the statistical defect distribution, defect type/shape (gas pores/rounded or lack of fusion/sharp and elongated), together with the defect location (surface or internal) are the main source of scatter in the fatigue data.

Considerable modelling efforts have been also undertaken to be able to predict the influence of key features (i.e., defects and residual stress profiles) on the fatigue life [12–15]. Most of the proposed models are based on existing ones and repurposed to consider the specificities of AMed materials. Specifically, fracture mechanics-based approaches yield good agreements when compared to the experimental data. Incidentally, the robustness of these approaches requires a detailed determination of the crack propagation rates and threshold.

In spite of all the aforementioned experimental and modelling efforts, it is still unclear which heat treatment post-processing scheme is more effective to obtain an optimal fatigue performance of defective PBF-LB AlSi10Mg materials. Early studies by Brandl et al. [16] and Domfang Ngnekou et al. [17] showed the potential benefit of the conventional T6 heat treatment on the fatigue properties of PBF-LB

* Corresponding author.
** Corresponding author.
E-mail addresses: itziar.serrano-munoz@bam.de (I. Serrano-Munoz), mauro.madia@bam.de (M. Madia).

https://doi.org/10.1016/j.matdes.2024.113170
Received 21 February 2024; Received in revised form 31 May 2024; Accepted 13 July 2024
Available online 15 July 2024

Nomenclature

Symbols

a	crack length
a_N	notch depth
a_0	El Haddad parameter in terms of crack length and considering the boundary correction factor
$\sqrt{area}$	Murakami's parameter
$\sqrt{area}_0$	El Haddad parameter in terms of $\sqrt{area}$ and considering the boundary correction factor
C	constant in the Basquin's equation
d_g	diameter of the gauge volume
F	cumulative probability
F_{max,V_c}	distribution of the largest defect in the volume V_c
h	thickness of the tubular surface volume
HV	Vickers' hardness
k	exponent in the Basquin's equation
l_1	length parameter in the cyclic R-curve equation
l_g	length of the gauge volume
$M(u)$	Mean Excess function
N	number of fatigue cycles
N_f	number of fatigue cycles to failure
n_s	number of exceedances in the volume scanned by means of μCT
P_f	probability of failure
$\bar{r}_d$	average radius of the killer defects measured in the fatigue samples
R	stress ratio
R_m	ultimate strength
$R_{p0.2}$	yield strength
T	return period
T_σ	scatter index in terms of applied stress
u	threshold in the Peak Over Threshold method
V_c	volume considered for the determination of the maximum defect distribution
V_s	volume scanned by means of μCT
V_{surf}	surface volume considered for the estimation of the killer defects distribution
$W_{\gamma,u,\sigma}$	Generalized Pareto Distribution
x_{max,V_c}	modal value of the largest defect in the volume V_c
δ	scale parameter of the Largest Extreme Value Distribution
γ	shape parameter of the Generalized Pareto Distribution
Φ	boundary correction factor
λ	location parameter of the Largest Extreme Value Distribution
ν_1	coefficient in the cyclic R-curve equation
σ	scale parameter of the Generalized Pareto Distribution
σ	applied stress
σ_e	fatigue limit for a general stress ratio
σ_{max}	maximum applied stress in a fatigue cycle
σ_{th}	threshold stress
σ_w	fatigue limit for complete reverse loading
Δa	crack extension
ΔK	stress intensity factor range
ΔK_p	plasticity-corrected stress intensity factor range
ΔK_{th}	fatigue crack propagation threshold
$\Delta K_{th,eff}$	effective fatigue crack propagation threshold
$\Delta K_{th,LC}$	long crack fatigue crack propagation threshold
$\Delta K_{th,op}$	extrinsic part of the fatigue crack propagation threshold
$\Delta\sigma$	applied stress range
$\Delta\sigma_e$	fatigue limit range for a general stress ratio
$\Delta\sigma_{exp}$	experimental fatigue limit range
$\Delta\sigma_{SC}$	fatigue limit range predicted by short crack models
$\Delta\sigma_{th}$	threshold stress range

Abbreviations

AB	As-Built
AM	Additive Manufacturing
GPD	Generalized Pareto Distribution
HCF	High Cycle Fatigue
HT1	Heat Treatment 1 (265 °C for 1 h)
HT2	Heat Treatment 2 (300 °C for 2 h)
LEVD	Largest Extreme Value Distribution
ME	Mean Excess
μCT	micro-Computed Tomography
POF	Probability Of Failure
POT	Peak Over Threshold

AlSi10Mg alloys. The authors argued that the homogenization of the microstructure and, in particular, the spheroidization of the eutectic Si-particles, could reduce both crack initiation and growth. Kempf et al. [18] also reported an improvement of the fatigue strength after T6 heat treatment for specimens tested at different stress ratios. On the contrary, Zhang et al. [19] concluded that T6, as well as annealing, have detrimental impact on the fatigue behavior compared to the as-built state. More recently, Tridello et al. [20] reported contrasting effects on the fatigue performance in the very high fatigue cycle regime, when applying different annealing treatments. In particular, they obtained an improved fatigue strength after annealing at 244 °C for 2 h, while the opposite trend was observed after annealing at 320 °C for 2 h. Note that the references introduced above are a small selection among the numerous studies available in the literature. For a broader view on all the studies published on the topic, the reader is referred to reviews such as [6–8,21].

The present study is aimed at investigating the influence of post-process low temperature heat treatments (< 320°C) on HCF behavior, in order to provide an in-depth understanding of the process-microstructure-performance relationship. The potential of different fracture mechanics approaches is also explored, including the Kitagawa-Takahashi diagram obtained by the El-Haddad model, Murakami's $\sqrt{area}$ approach, and cyclic R-curve analysis.

2. Materials and methods

2.1. Fabrication of the specimens and heat treatments

The full description of the process and process parameters, as well as the thorough characterization of the microstructure and residual stresses, have been presented in previous studies by the authors [22,23,50]. Therefore, this section is intended to provide a concise summary of the main material information for the sake of understanding.

Table 1
Process parameters.

	Present work [22,23]	Beretta et al. [15]
PBF-LB/M Machine	Concept Laser M2	EOS M280
Power, W	380	370
Hatch space, mm	0.1	0.19
Scan speed, mm/s	1500	1300
Layer thickness, μm	30	30
Temperature of the build plate, °C	200	100

The PBF-LB/M process parameters are reported in Table 1. As the fatigue data obtained in this work will be compared to those from a benchmark activity by Beretta et al. [15], also the process parameters from [15] are reported in Table 1. In fact, most of the parameters are very close to each other. Nevertheless, it must be enphasized that the preheating temperature of the build plate was significantly different. A build plate temperature of 100 °C is considered to lead to a minor reduction of the residual stress [24], whereas preheating at 200 °C provides almost full relaxation [23,25]. In general, a meaningful mitigation of residual stresses is reached by using a preheating temperature of 150 °C, at least.

Cylindrical bars with a diameter of 13 mm and a length of 134 mm were fabricated with their axes parallel to the build direction (Fig. 1a). A total of 36 pieces were produced in the same batch. Before machining the specimens to the final shape for the fatigue testing (Fig. 1b), post-process heat treatments were conducted.

We already reported the effectiveness of two low-temperature heat treatments (265 °C for 1 h and 300 °C for 2 h) on improving the crack growth resistance of the PBF-LB/M AlSi10Mg compared to the as-built state [22]. This is believed to be related to the microstructural changes, which lead to improvement in ductility, and development of extrinsic resistance mechanisms, such as crack closure. A summary of the microstructural evolution occurring in the alloy upon each heat treatment is schematically depicted in Fig. 2. In the as-built condition the microstructure consists of α-Al cells decorated by an ultra-fine eutectic Si-network. Potentially, part of the Si can be found as excess (supersaturated condition), as well as in the form of nano-sized Si particles in the α-Al cells [26]. The main microstructural change observed upon heating at 265 °C for 1 h (named HT1 in the following) is the precipitation of the Si excess and the enlargement of the size of the α-Al cells. This scheme is selected because it is thought to provide the maximum stress relaxation before the silicon network starts disaggregation. The second heat treatment carried out at 300 °C for 2 h (HT2) is characterized by the disaggregation of the Si-network into micrometric particles. This scheme is typically used for stress relief. Finally, heating at temperatures higher than about 450 °C leads to the further coarsening of the Si particles, thermally induced porosity, and the formation of Fe-intermetallics [27,28].

The heat treatments were performed using 24 out of 36 specimens, 12 for HT1 and 12 for HT2 respectively. The specimens were polished after the heat treatments, according to the standard ISO 1099 [29]. A longitudinal mechanical polishing was applied using a pad with abrasive diamond paste to minimize the surface roughness.

2.2. Characterization of the defect distribution

The Murakami's $\sqrt{area}$ parameter, i.e., the square root of the projected area of the defect onto the plane perpendicular to the maximum principal stress, is often used as an effective quantitative measure of the defect size [30]. This parameter has been successfully used for the definition of the size of any kind of defect type in AMed materials [15,31,32].

The characterization of the defect distribution was conducted by performing micro–Computed Tomography (μCT) scans of the gauge volume of the specimens prior to fatigue testing (Fig. 3a). The voxel size was 8 μm, which therefore defined the resolution limit of the dataset. The software VGSTUDIO MAX 3.0 [33] was used to process and visualize the datasets. Preliminary analyses of the μCT scans revealed the high density of the specimens (99.95 %) and the predominant presence of gas porosity (94 %) compared to lack of fusion (LOF, 6 %). It is important to remind at this stage that the latter are "pancake-shaped" defects which are more detrimental to fatigue strength than spherical gas pores, assumed that the equivalent size is equal [34].

The statistical analysis of the defect distribution was based on the Peak Over Threshold (POT) methodology [35] because (i) it cuts-off the values close to the resolution of μCT device and (ii) it provides a correct representation of the upper tail of the defect distribution, which is the most meaningful to the fatigue limit, defined as non-propagating condition of the largest defect. The method considers the defect sizes (in terms of $\sqrt{area}$) above a defined threshold u, which are therefore defined as exceedances. The value $\sqrt{area} - u$ defines the excesses. The Generalized Pareto Distribution (GPD) $W_{\gamma,u,\sigma}$ is appropriate to describe the statistical distribution of the excesses, where γ and σ are the shape and scale parameter, respectively. In this study, it was assumed $\gamma \to 0$, therefore the GPD reduces to an exponential distribution ($W_{\gamma,u,\sigma} \to W_{0,u,\sigma}$):

$$W_{0,u,\sigma} = 1 - \exp\left(-\frac{\sqrt{area} - u}{\sigma}\right) \quad (1)$$

The choice of the threshold u where the GPD provides a correct

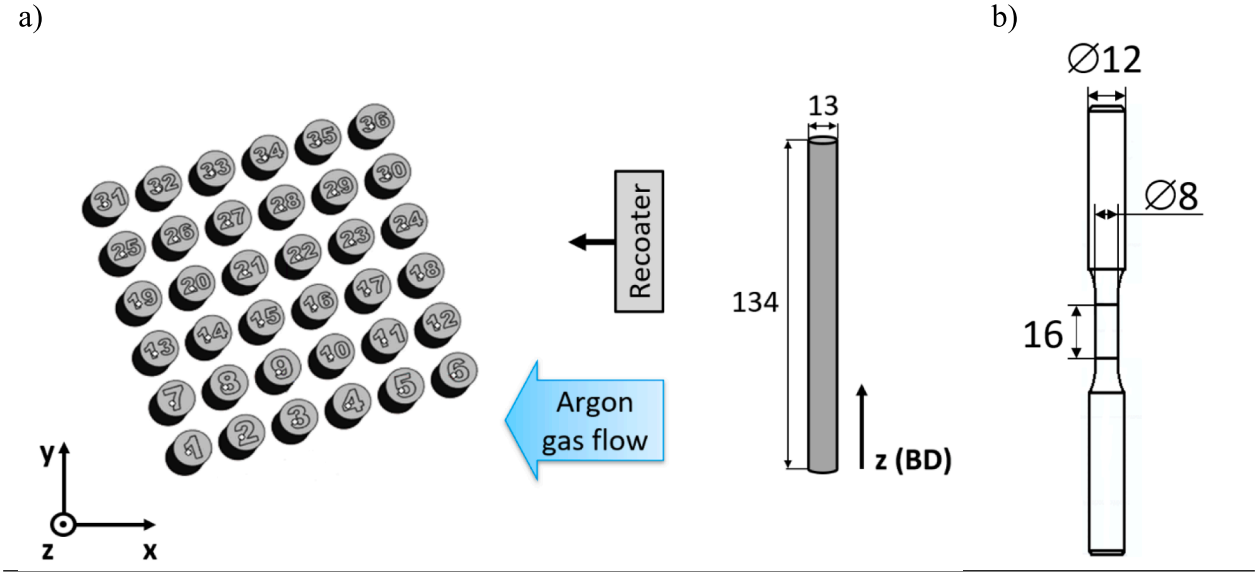

Fig. 1. Fabrication of the fatigue specimens: a) Schematic of the PBF-LB/M sample arrangement within the build chamber; b) Final shape of the fatigue specimens after machining.

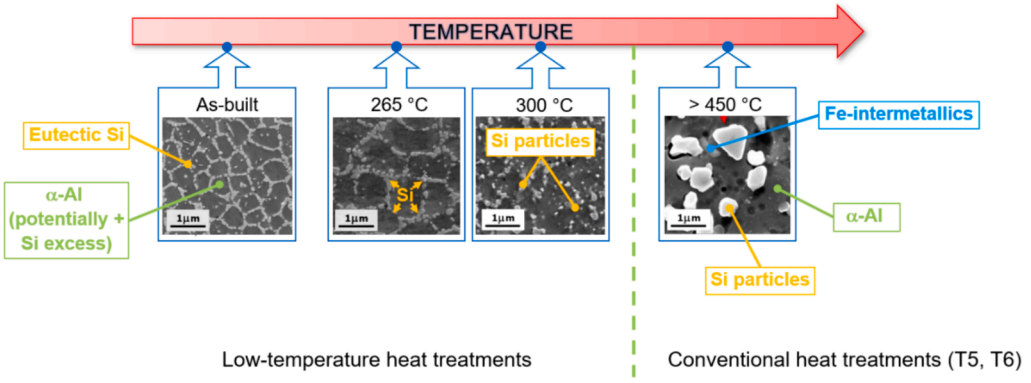

Fig. 2. Influence of different heat treatments on the microstructural evolution of the investigated PBF-LB/M AlSi10Mg.

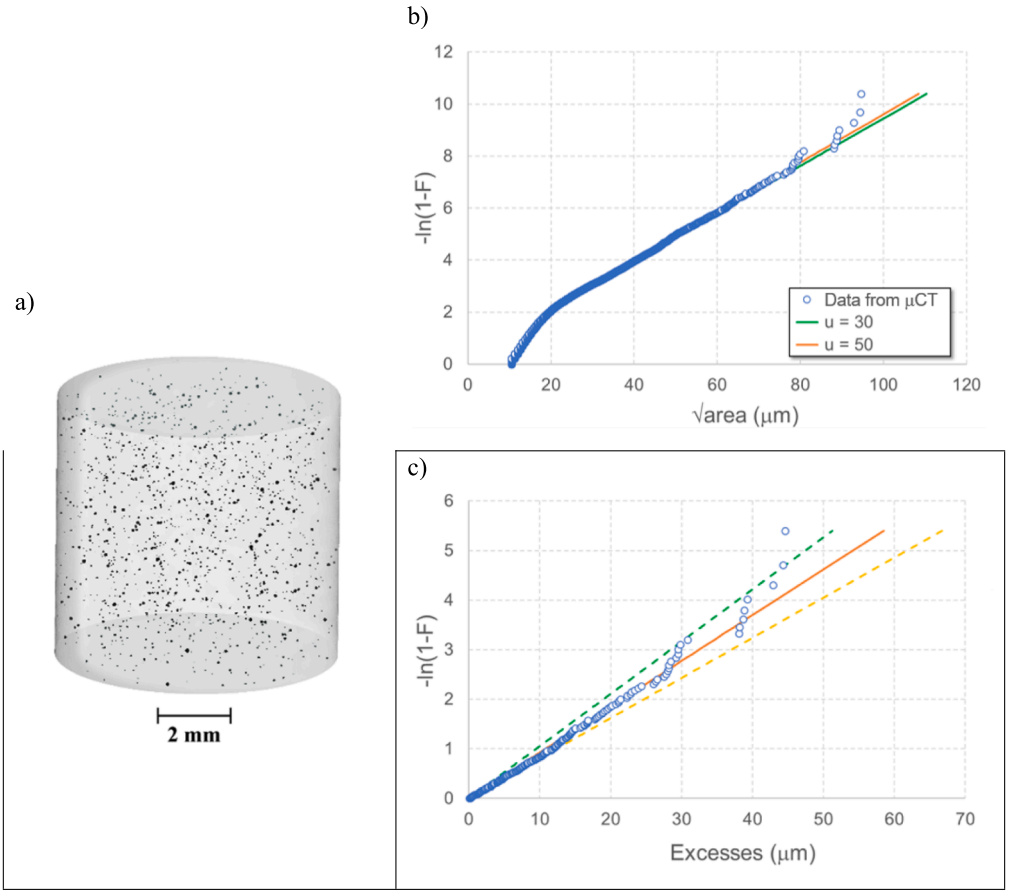

Fig. 3. Determination of the statistical distribution of defects: a) µCT scan of a gauge volume of a fatigue specimen; b) exponential distribution probability plot for the dataset, where 2 distributions for 2 threshold values are plotted together with the experimental data; c) probability plot of the excesses $\sqrt{area} - u$, where $u = 50$ µm and the dashed lines represent the lower and the upper bound of the 95 % confidence band.

approximation of the excess distribution is crucial in the POT method. A graphical representation using a probability plot of the exponential distribution is usually enough to get a rough estimate (Fig. 3b). A more rigorous methodology is based on the evaluation of statistical estimators such as the mean excess (ME) function [36] defined as:

$$M(u) = \frac{\sum_{i=1}^{n} (\sqrt{\text{area}}_i - u) I_{[\sqrt{\text{area}}_i > u]}}{\sum_{i=1}^{n} I_{[\sqrt{\text{area}}_i > u]}} \quad (2)$$

The value, above which the mean excess plot is linear, defines the correct estimate for u. The estimations carried out in this study showed that a minimum threshold $u = 30$ µm is already enough to get an accurate estimation of the upper tale of the defect distribution. The choice of higher thresholds has just a minimal effect on the asymptotic distribution, as showed by the probability plot reported in Fig. 3b, where the GPD has been determined for $u = 30$ µm (scale parameter $\sigma = 11$ µm) and $u = 50$ µm (scale parameter $\sigma = 10.8$ µm). The probability plot of the excesses for a threshold $u = 50$ µm is depicted in Fig. 3c, where almost all experimental values fall within the 95 % confidence band.

The approximation of the upper tale of the defect distribution obtained by the POT analysis is very useful to estimate the distribution of the killer defects [26,30]. Given the number of exceedances n_s in the scanned volume V_s, the return period T of the maximum defect in a volume V_c is defined as:

$$T = \frac{n_s}{V_s} \bullet V_c \tag{3}$$

assuming a constant defect density. Applying the rules of the extreme values statistics, and considering that the excesses are well-described by an exponential distribution, the distribution of the largest defect in V_c can be approximated by a Gumbel distribution:

$$F_{\max,V_c} \approx \exp\left[-\exp\left(-\frac{\sqrt{\text{area}} - x_{\max,V_c}}{\sigma} \right) \right] \tag{4}$$

where $x_{\max,V_c}$ is the modal value of the maximum defect in the volume V_c:

$$x_{\max,V_c} = u + \sigma \bullet \ln(T) \tag{5}$$

A crucial issue for the application of the method to the estimation of the killer defects distribution is the correct definition of the volume V_c. It is common knowledge, that most of the fatigue failures in AMed materials originate from surface defects, unless large bulk defects are present. Therefore, the authors in [26] and [30] proposed that the size of the killer defect should be estimated as the maximum defect in a surface volume V_{surf}. In case of cylindrical specimens, V_{surf} is a tubular volume given by

$$V_{surf} = \frac{\pi}{4} \bullet l_g \bullet \left[d_g^2 - (d_g - 2 \bullet h)^2 \right] \tag{6}$$

where l_g and d_g are respectively the length and the diameter of the gauge volume, and h is the thickness of the tubular volume. The latter is calculated as $\bar{r}_d/0.8$, where $\bar{r}_d$ is the average radius of the killer defects measured in the fatigue samples.

2.3. Experimental determination of the fatigue properties

High cycle fatigue (HCF) tests were performed using a uniaxial servohydraulic Schenck 25kN testing machine at a load ratio of $R = 0.1$ and a frequency of 30 Hz in force-control mode, according to the standard ISO 1099 [29]. Stress amplitudes between 35 and 105 MPa were investigated, which correspond to a fatigue life range between $10^3 - 10^7$ cycles. The specimens that survived at 10^7 cycles were considered run-out (operational definition of the fatigue limit) and retested at the highest stress level, namely at a load which gave a failure in the range of $10^3 - 10^4$ cycles to minimize the influence of accumulated damage (assumed to be negligible, see [37]). About seven specimens were tested for each material condition (AB, HT1 and HT2). Further three specimens per each material state were used to perform strain-controlled fatigue tests to determine the cyclic stress strain curve (not reported here). Finally, the Basquin model was fitted to the data in the finite life regime:

$$N \bullet \Delta\sigma^k = C \tag{7}$$

No tests were conducted to determine the fatigue limits for the investigated material conditions because it is not possible to determine values for flawless AMed materials. Instead, the fatigue limits were estimated from the basic quasi-static mechanical properties of the materials reported in [22]. First, the fatigue limit for complete load reversal ($R = -1$) was derived from the Vickers hardness according to the following relationship:

$$\sigma_w = (1.6 \pm 0.1) \bullet HV \tag{8}$$

This relationship is generally used for steels and its accuracy for non-ferrous metals is claimed to be questionable, also because non-ferrous metals such as aluminum alloys do not have a defined fatigue limit. Nevertheless, Murakami demonstrated in [30] that Eq. (8) can be applicable to some non-ferrous metals, claiming that the hardness of the microstructure is the crucial factor controlling the fatigue strength of non-ferrous metals, as well as of steel.

Then, a mean stress correction based of a Goodman-Haigh diagram was used to obtain the values of the fatigue limits σ_e at $R = 0.1$. In particular, the modified Goodman line and the yield envelope were considered. The mean values of the basic mechanical properties and the estimated fatigue limits are reported in Table 2.

As the fatigue resistance and the associated scatter are strictly dependent on the propagating/non-propagating condition of the largest defect in the material (the so-called killer defects), the fracture surface of every tested specimen was analyzed.

2.4. Prediction of the fatigue limit based on short crack models

The prediction of the fatigue limit in presence of defects is essential for the qualification of safety relevant components. Murakami demonstrated that the fatigue limit is the threshold stress σ_{th} of non-propagating cracks generated at the tip of defects [30]. This concept holds true even in the definition of the intrinsic material fatigue limit for smooth fatigue specimens, as demonstrated in [38]. The relationship between the fatigue limit and defect size is usually represented by the Kitagawa-Takahashi Diagram [39]. In their original proposal, Kitagawa and Takahashi defined the region of infinite life (or region of non-propagating cracks) as the area below the threshold conditions given by the material endurance limit $\Delta\sigma_e$, and the fatigue crack growth threshold $\Delta K_{th,LC}$, which rewritten in terms of the threshold stress range $\Delta\sigma_{th}$ gives:

$$\Delta\sigma_{th} = \begin{cases} \Delta\sigma_e & \text{for} a < a_0 \\ \dfrac{\Delta K_{th,LC}}{\Phi \bullet \sqrt{\pi a}} & \text{for} a \geq a_0 \end{cases} \tag{9}$$

where Φ is the boundary correction factor and $a_0 = 1/\pi \bullet \left[\Delta K_{th,LC}/(\Phi \bullet \Delta\sigma_e)\right]^2$ defines the sharp transition between short and long cracks. A graphical representation of the threshold stress according to Kitagawa-Takahashi is shown in Fig. 4. To avoid a sharp transition in the short crack regime, which is not representative of the real material behavior, El Haddad et al. proposed a relationship to ensure a smooth transition between the region of microstructural short cracks (intrinsic endurance limit) and the region of long cracks [40,41]:

$$\Delta\sigma_{th} = \Delta\sigma_e \bullet \sqrt{\frac{a_0}{a + a_0}} \tag{10}$$

A comparison between the El Haddad model and the original one by Kitagawa-Takahashi is presented in Fig. 4. Note, that the relationships given in Eqs. (9) and (10) can be modified by substituting the crack length a with the Murakami's $\sqrt{\text{area}}$ parameter [30].

Although the approximation provided by the El Haddad model proved to work very well also for AMed materials [42], the model suffers from weak points, namely it does not consider the mechanisms which lead to crack arrest/propagation (correct definition of the fatigue limit), and it has a predefined shape. In contrast, the use of short crack models enables the correct consideration of extrinsic toughening mechanisms which are developed during crack propagation, already from the stage of mechanically-physically short cracks [43]. This feature, together with the possibility of considering nearly every stress distribution (e.g., stress at notches), yields the benefit of extending the range of use of short crack models to the prediction of the component fatigue limit.

Most of the short crack models are based on the so-called cyclic R-

Table 2
Basic mechanical properties according to [22] and estimated fatigue limits.

Condition	$R_{p0.2}$(MPa)	R_m(MPa)	HV(kgf/mm^2)	σ_w(MPa)	σ_e(MPa)
AB	178	338	86	138	80
HT1	158	297	80	128	71
HT2	123	217	69	110	55

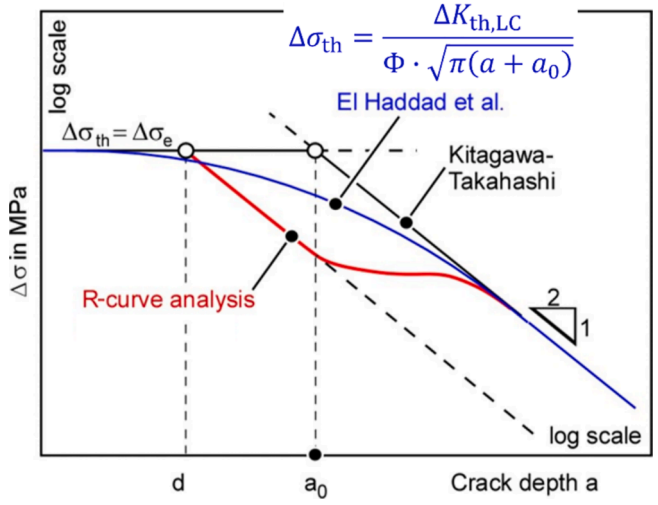

Fig. 4. Kitagawa-Takahashi diagram. Comparison of the fatigue limit prediction given by different models. Short crack models (i.e., R-curve analysis) provide the most conservative estimations.

curve (see [44–46] for reference), which describes the dependence of the crack propagation threshold ΔK_{th} on crack extension Δa in the mechanically-physically short crack regime [47]:

$$\Delta K_{th}(\Delta a) = \Delta K_{th,eff} + \Delta K_{th,op}(\Delta a) \tag{11}$$

where $\Delta K_{th,eff}$ is the intrinsic crack propagation threshold and $\Delta K_{th,op}$ is the opening or extrinsic part of the fatigue crack propagation threshold, which incorporates the effect of extrinsic toughening mechanisms (e.g., closure effects) and depends on the crack extension Δa.

Two different methods based on short crack models were considered in this work: (i) the method by Maierhofer et al. [48], which accounts for the finite crack-like notch depth in a modified formulation of the Kitagawa-Takahashi diagram; and (ii) the cyclic R-curve method first proposed by Tanaka and Akiniwa [44], which is based on the comparison of the crack driving and resistance force for the determination of the non-propagating condition for short cracks. A brief description of the models is given in the following for the sake of comprehension.

Maierhofer et al. questioned the approximation of the threshold stress range in the El Haddad model, as it does not consider the build-up of closure in the short crack regime, thus providing non-conservative estimates. Another crucial weak point is the non-consideration of the influence of the depth of pre-existing flaws, which is also a problem in the approach by Chapetti [46]. The authors in [48] proposed a modification of the threshold stress range which incorporates the gradual build-up of the crack closure (cyclic R-curve) and the notch depth a_N:

$$\Delta\sigma_{th}(a_N, \Delta a) = \min\left(\frac{\Delta K_{th}(\Delta a)}{\Phi \bullet \sqrt{\pi(a_N + \Delta a)}}, \Delta\sigma_e\right) \tag{12}$$

which is limited by the endurance limit for very short total crack lengths. Note that this formulation can be applied just to sharp or crack-like notches. The function $\Delta\sigma_{th}(a_N, \Delta a)$ provides limiting curves for non-propagating cracks for different notch depths as shown in Fig. 5a. Each limiting curve starts at $\Delta\sigma_{th} = \Delta K_{th,eff}/(\Phi \bullet \sqrt{\pi a_N})$, which corresponds to the initial closure-free condition. As the crack grows, the closure builds up and the deeper the notch, the steeper is the initial increase of the limiting curve. As the crack grows away from the notch, it approaches the long crack regime ($\Delta K_{th,LC}$) asymptotically. The fatigue limit for a given notch $\bar{a}_N$ is given by the maximum allowable threshold stress in the corresponding limiting curve:

$$\max(\{\Delta\sigma_{th}(\bar{a}_N, \Delta a) : \Delta a = 0 \rightarrow \infty\}) \tag{13}$$

represented by the green circles in Fig. 5a. The maximum non-propagating crack length is obtained as well.

The principle of the resistance curve method introduced by Tanaka and Akiniwa is schematically depicted in Fig. 5b. It is assumed that a short stage II crack growing from a notch is closure free, which means that its initial crack propagation threshold is equal to $\Delta K_{th,eff}$. As the crack grows out of the notch, crack closure effects are built up and the fatigue crack growth resistance increases according to the cyclic R-curve. The crack driving force of the growing crack is plotted in the same diagram, as reported in Fig. 5b. Note that two important aspects must be considered when comparing the cyclic R-curve method by Tanaka and Akiniwa, and the method by Maierhofer et al. First, the proper

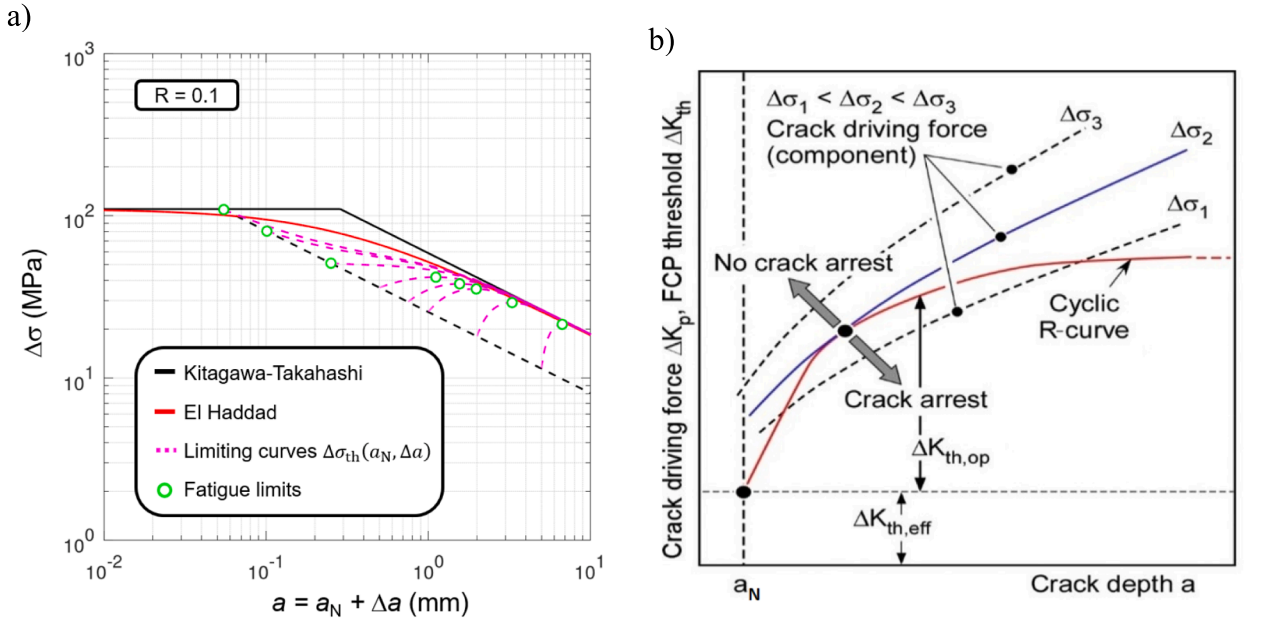

Fig. 5. Determination of the Kitagawa-Takahashi diagram by short crack models: a) Method by Maierhofer et al. [48] (modified from and applied to the AMed AlSi10Mg investigated in this study); b) Resistance curve (cyclic R-curve) method introduced by Tanaka and Akiniwa (modified from [44]).

calculation of the crack driving force for mechanically-physically short crack should be carried out considering an elastic–plastic fracture mechanic parameter like the plasticity corrected stress intensity factor ΔK_p [43], as shown in Fig. 5b. Nevertheless, to ensure the comparison with the methodology by Maierhofer et al., the linear elastic fracture mechanics parameter ΔK was used in this work. Secondly, the cyclic R-curve method is not limited to sharp notches, as the crack driving force can be calculated even for cracks emanating from blunt notches. Finally, the fatigue limit for a given notch is given by the stress at which the largest crack emanating from the notch-tip still arrests ($\Delta\sigma_2$ in Fig. 5b), thus defining the maximum allowable non-propagating crack. This means that the Kitagawa-Takashi diagram, as depicted in Fig. 5a, can be obtained from the estimation of the fatigue limits and non-propagating crack lengths by applying the resistance curve method for increasing notch depths.

Given the assumptions of considering sharp notches and linear elastic fracture mechanics parameters, it is believed that both methods should provide the same results in terms of fatigue limits and non-propagating crack lengths.

3. Results and discussion

3.1. Fatigue tests

The results of the whole fatigue tests conducted on the PBF-LB/M AlSi10Mg are presented in Fig. 6. Here, the failed specimens are marked by full points, while the runouts at 10^7 cycles are depicted with open circles. Unlike the fatigue crack propagation tests reported in [22], the fatigue tests did not show a clear trend among the datasets related to the different material conditions. The material in the heat-treated conditions clearly did not outperform the AB material state. The fatigue data seem to fall well within a scatter band calculated for a failure probability (P_f) between 10 % and 90 % ($T_\sigma = \sigma_{90\%}/\sigma_{10\%} = 1.26$), therefore just one Basquin line was fitted to the whole fatigue data.

It is important to notice that the data for HT1 and HT2 in the upper part of the finite life regime are characterized by a maximum applied stress $\sigma_{max} = \Delta\sigma/(1-R)$, which lies above the yield strength. This is believed to be one of the main reasons for the poor fatigue performance of HT1 and HT2 at higher stresses. The further reason for the scatter in the fatigue data is related to the values of the killer defects found in each specimen at the fracture origin. Every specimen failed because of a crack starting at a gas pore located at the surface of the specimens. Fig. 6 points out clearly that specimens tested at the same stress level could have very different fatigue lives if the killer defects had different sizes. Larger defects resulted in shorter lives. Nevertheless, it must be noted that just one specimen per stress level for each material condition has been tested in this work, so that the influence of the microstructure cannot be ruled out at this stage. This issue will be clarified in Section 3.2 based on the analysis of the scatter of fatigue data. The data shown in Fig. 6 are reported in Table 4 of Section 3.2.

Furthermore, the results were compared to the ones obtained by Beretta et al. [15], whereby only the fatigue tests on AB and machined specimens were considered. Fig. 6 shows that the results in [15] slightly outperform the fatigue data obtained in this work. The possible reason could reside either in a different population of killer defects, or in the influence of residual stress and/or microstructure. Therefore, to prove the first hypothesis, the killer defect sizes were measured by fractographic analyses of the fracture surfaces of the fatigue specimens examined by means of a digital microscope Keyence VHX-7000 N. Some examples of killer defects are depicted in Fig. 7. The Largest Extreme Value Distribution (LEVD) was fitted to the experimental data and compared to the distribution reported in [15]:

$$F = \exp\left[-\exp\left(-\frac{\sqrt{\text{area}}-\lambda}{\delta}\right)\right] \tag{14}$$

The probability plot is given in Fig. 7, while the LEVD parameters λ and δ are provided in Table 3. First, the killer defects are well represented by a LEVD, being all experimental points well within the 95 % confidence band. Secondly, there is nearly no difference between the LEVD fitted to the data obtained in this work and the LEVD determined by Beretta et al. [15], thus demonstrating that it is unlikely that the difference in fatigue performance stemmed from different populations of defects. Fig. 7 also shows the killer defect distribution estimated by means of the extreme value statistics reported in the Section 2.2. The POT estimates were obtained considering a surface volume $V_{surf} \approx 19.7$ mm^3, being the average killer defect radius $\bar{r}_d \approx 40$ µm, the diameter of the gauge

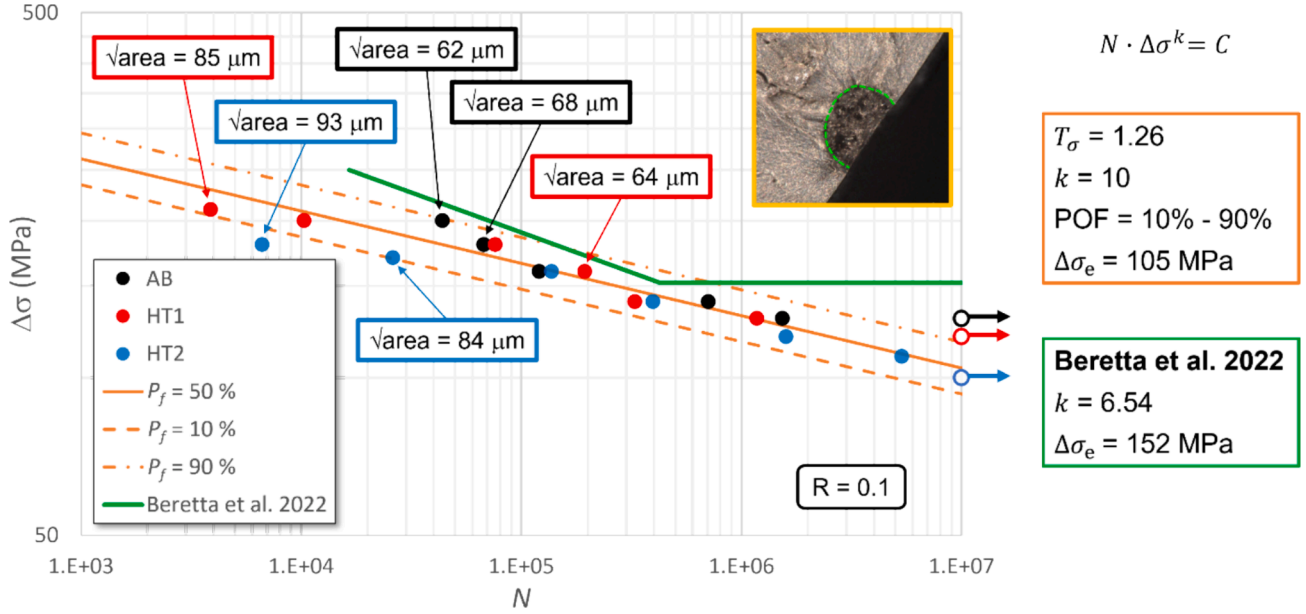

Fig. 6. Results of the fatigue tests conducted on the AMed AlSi10Mg alloy. The results of three different datasets corresponding to the three material conditions considered in this study (AB, HT1 and HT2) are presented (failures correspond to full points, while runouts are represented by circles with arrows). The sizes of selected killer defects for specimens tested at different stress levels are provided. The results of the fatigue tests carried out by Beretta et al. [15] on smooth specimens are shown for comparison.

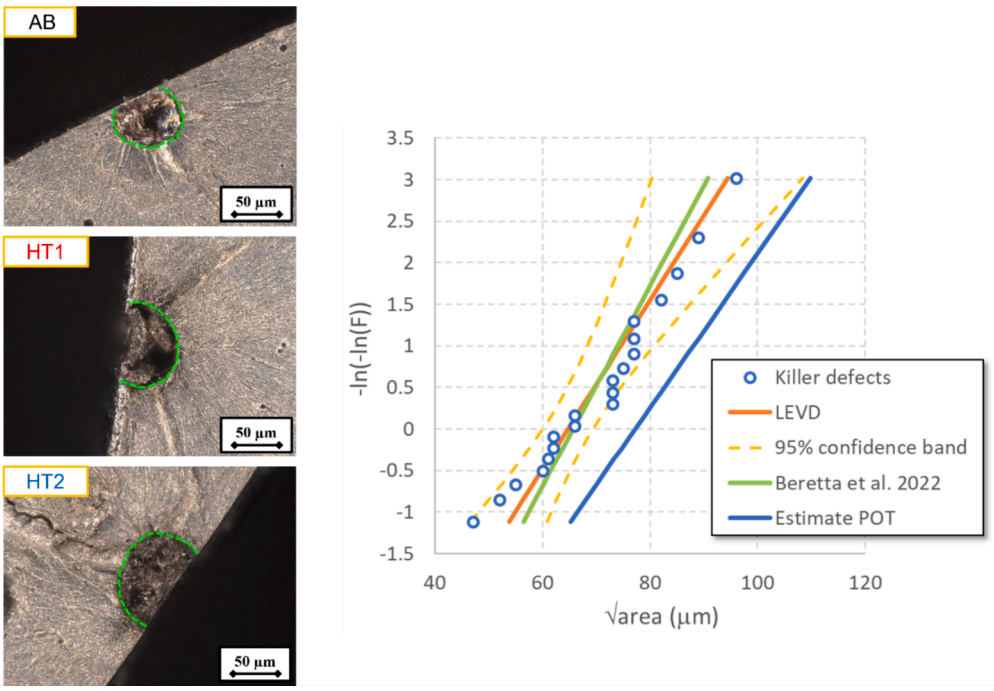

Fig. 7. Statistical distribution of the killer defects determined by fractographic observation of the fracture surface of the broken fatigue specimens. As expected, all the defects were gas round pores and were located at the surface of the specimens in the gauge length. The comparison of the LEVD (Largest Extreme Value Distribution) fitted to the experimental killer defect distribution with the distribution published by Beretta et al. [15] shows good agreement. The POT provided a conservative estimate of the largest defects in the surface volume.

Table 3
LEVD parameters.

	Present work	Beretta et al. [15]
λ(µm)	64.7	65.7
δ(µm)	9.8	8.3

volume $d_g = 7.93$ mm and the length of the gauge volume $l_g = 16$ mm. While a good approximation of the scale parameter of the distribution was obtained, the location parameter (modal value of the largest defects) was slightly overestimated, so that the estimated distribution was conservative compared to the experimental distribution of the killer defects.

The second hypothesis, namely the influence of residual stress and/or microstructure, could explain this difference. Beretta et al. [15] reported surface compressive residual stress as high as −76 MPa for the machined specimens, whereas Sausto et al. [49] reported surface residual stress values between −50 and −100 MPa for specimens machined by lathe and subsequently finished by emery paper. Within the frame of our study, surface residual stress measurements performed in single edge notch bending (SENB) specimens using the same machining process as the one used for the HCF samples also yield compressive residual stresses at the surface/subsurface (average of −75 MPa). Furthermore, no significant differences in magnitudes are observed between the three investigated conditions (i.e., as-built, HT1, and HT2 [50]). Therefore, the most plausible hypothesis for the slight increase in fatigue life reported in [15], when compared to our study, would be the slight difference in the as-built microstructure: higher cooling rates resulting from a lower build temperature (100 °C against 200 °C) leads to smaller average size of the α-Al cells and increased yield strength (258.4 MPa [15] against 178 MPa for the as-built condition of our study). In other words, microstructural changes of the as-built would have a higher influence in fatigue life than changes induced by low temperature heat treatments.

3.2. Normalized S-N curves

It has been already stated that the presence of manufacturing defects is the major source of scatter in fatigue data of AMed materials. Murakami showed that, in case of materials containing defects, the correct driving force is not the absolute value of the applied stress σ, but rather its value relative to the threshold stress (or fatigue limit) σ_{th} of the killer defect contained in the specimen [30,51]. Therefore, this methodology was applied to the data given in Fig. 6 and the results are presented in Fig. 8 and Table 4. It is important to mention that the threshold stress range $\Delta\sigma_{th}$ for every killer defect and material condition was estimated according to the El Haddad expression, also reported in Fig. 8. Here, the boundary correction factor $\Phi = 0.65$ was selected according to Murakami [30], because all killer defects were surface defects. A clear trend can be seen by the data plotted in Fig. 8, where the datasets of HT1 and HT2 fall in the same narrow scatter band ($T_\sigma = 1.12$), thus confirming that the scatter of fatigue data can be attributed predominantly to the scatter of manufacturing defects. Note that the normalization worked well also for the upper part of the finite life regime of HT1 and HT2 conditions, whereby the maximum applied stress was higher than the yield strength of the material. The AB data show a better fatigue performance in the normalized plot, which means that the ratio between fatigue strength and threshold stress is higher for AB material compared to HT1 and HT2, considering an equivalent defect size. This result might be an indicator of the influence of microstructure on crack initiation. Future work is needed to confirm this preliminary hypothesis.

The same type of analysis was conducted for the data within the same set (i.e., specimens with the same material condition) to demonstrate the influence of process defects on the fatigue scatter when the microstructural variation is ruled out. The values given in Table 5 show a reduction of the scatter (T_σ) for normalized data, where the threshold stress for each killer defect is considered.

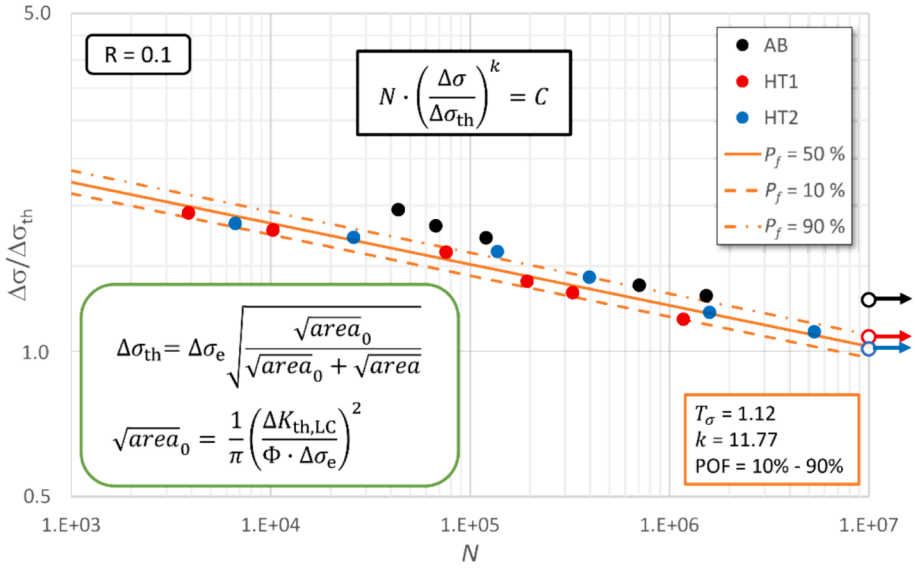

Fig. 8. Normalized S-N diagram: When the applied stress range $\Delta\sigma$ is normalized by the fatigue limit of the corresponding killer defect $\Delta\sigma_{th}$, the scatter is significantly reduced.

Table 4
Summary of the fatigue test results.

	$\Delta\sigma$(MPa)	N_f	$\sqrt{area}$(μm)	$\Delta\sigma_{th}$(MPa)	$\Delta\sigma/\Delta\sigma_{th}$
AB	200	43,700	62.0	102.0	1.962
	180	67,316	68.0	99.1	1.816
	160	120,482	82.5	93.2	1.717
	140	706,175	61.2	102.3	1.368
	130	1,532,958	66.4	99.9	1.302
	130	10,000,000	62.0	102.0	1.275
HT1	210	3874	85.4	108.7	1.931
	200	10,281	72.6	112.3	1.782
	180	76,004	72.6	112.3	1.603
	160	193,641	64.4	114.7	1.395
	140	327,412	96.1	106.0	1.320
	130	1,174,921	74.5	111.7	1.164
	120	10,000,000	72.6	112.3	1.069
HT2	180	6637	93.0	98.0	1.836
	170	26,039	84.5	99.0	1.718
	160	137,131	79.0	99.6	1.607
	140	396,002	88.8	98.5	1.422
	120	1,589,833	77.3	99.8	1.203
	110	5,336,296	72.5	100.3	1.096
	100	10,000,000	84.5	99.0	1.010

Table 5
Scatter index for original ($\Delta\sigma$) and normalized ($\Delta\sigma/\Delta\sigma_{th}$) data.

	T_σ $\Delta\sigma$	$\Delta\sigma/\Delta\sigma_{th}$
AB	1.110	1.045
HT1	1.128	1.079
HT2	1.115	1.112

3.3. Prediction of the fatigue limit

Short crack models were applied to the prediction of the fatigue strength. The models rely on the determination of the fatigue crack propagation threshold in the regime of the mechanically-physically short cracks, which is well defined by the cyclic R-curve. The experimental determination of the cyclic R-curve for the material conditions presented in this work was explained extensively in [22]. Nevertheless, the mathematical formulation of the cyclic R-curve was simplified to the following expression in this work:

$$\Delta K_{th}(\Delta a) = \Delta K_{th,eff} + \left(\Delta K_{th,LC} - \Delta K_{th,eff}\right) \bullet \left(1 - \nu_1 \bullet e^{-\frac{\Delta a}{l_1}}\right) \quad (15)$$

where the material parameters for each condition are given in Fig. 9. Here, even the simplified formulation of the cyclic R-curve can capture the fatigue resistance behavior of the three investigated conditions in the short crack regime. Further, the cyclic R-curve gives the gradual build-up of the closure effect in terms of crack extension Δa, whereas the defect size is defined in terms of the Murakami's $\sqrt{area}$ parameter. Therefore, it is assumed that a crack emanating from a surface pore evolves as a semi-circular crack ($\sqrt{area} = \sqrt{\pi/2} \bullet a$), resulting in the following expression for the applied crack driving force:

$$\Delta K = 0.65 \bullet \Delta\sigma \bullet \sqrt{\pi \bullet \sqrt{area}} = 0.728 \bullet \Delta\sigma \bullet \sqrt{\pi \bullet a} \quad (16)$$

Many authors demonstrated the applicability of Eq. (16) to defects in AMed materials (see [15,31,32]).

The results of the application of the short crack models are presented in Fig. 10. In general, all the models work well for the dataset related to the different material conditions. As expected, short crack models provide a more conservative estimate of the region of non-propagating cracks, which is clearly shown by the comparison of the predicted fatigue limits reported in Table 6. The comparison between the short crack models shows that these are fully equivalent and provide the same results both in terms of fatigue limit and non-propagating crack size.

All in all, it is shown that the size of non-propagating defects is below 30 μm, which is in line with some other findings reported for the as-built condition [32,52,53]. The focus is now on the optimization of the as-built microstructure to improve the trade-off between residual stress mitigation and tensile strength [54,55]. The gain in strength obtained by applying direct ageing (DA, T>160 °C, see for e.g., [56]) seems to overcome the deleterious effect of not fully alleviating tensile residual stress at the surface [57,58]. This fact is even more relevant when the material would be subjected to further surface post-processing, such as machining [59–61]. In addition, using the DA in comparison to conventional T6 heat treatments has the advantage of avoiding the development of thermally induced porosity [62].

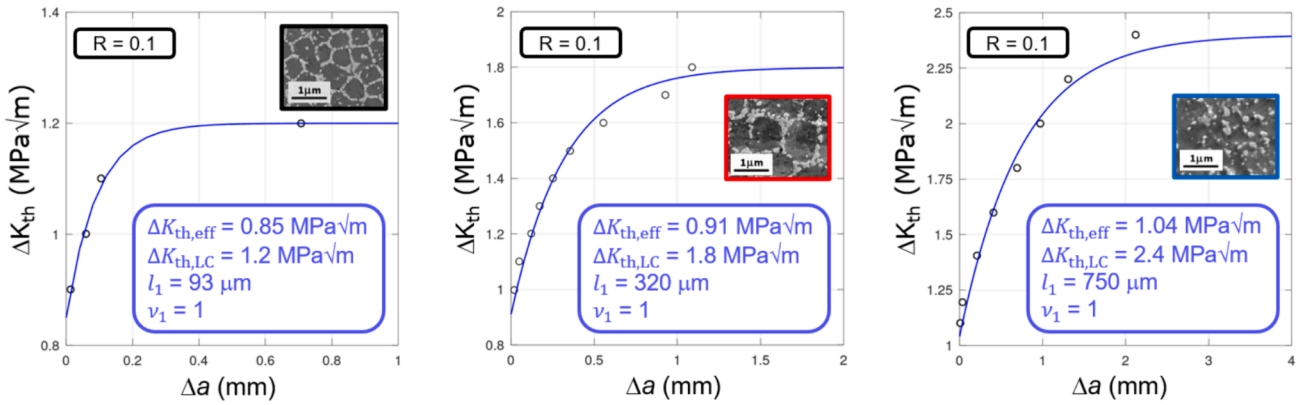

Fig. 9. Cyclic R-curves determined for the different material conditions: As-built (left), after HT1 (center) and after HT2 (right). The black circles refer to the experimental dataset, whereas the curves are obtained by fitting the Eq. (11) to the experimental points.

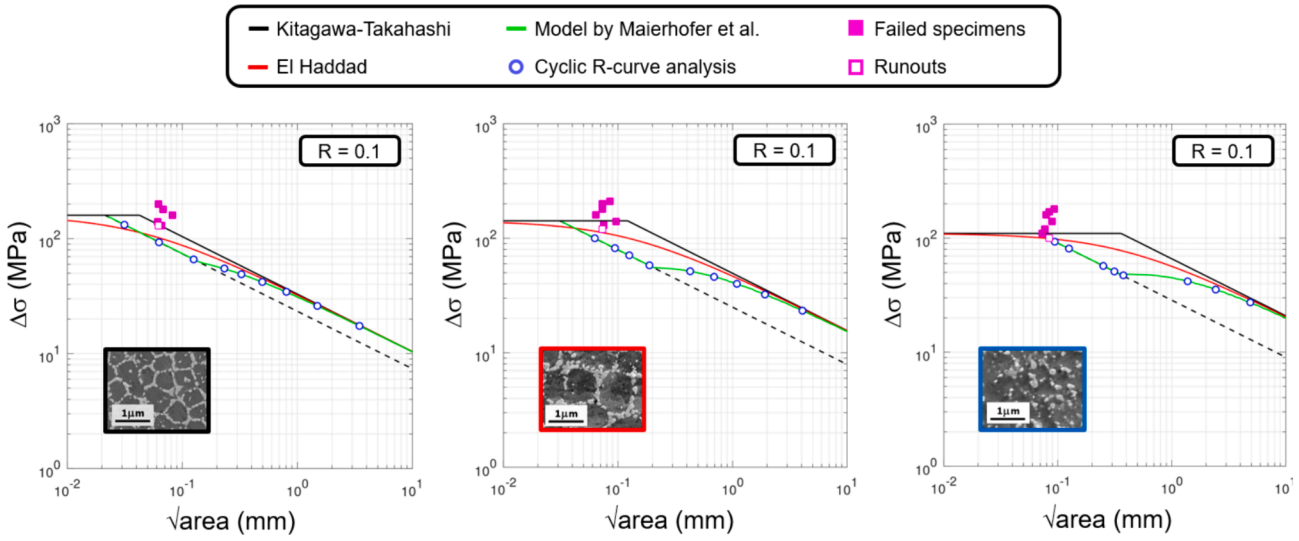

Fig. 10. Kitagawa-Takahashi diagrams for the different material conditions: As-built (left), after HT1 (center) and after HT2 (right). All the models presented in this work give satisfactory predictions of the threshold stress, whereby short crack models are the most conservative.

Table 6
Prediction of the fatigue limit by the El Haddad model ($\Delta\sigma_{th}$) and short crack models ($\Delta\sigma_{SC}$). As expected, short crack models provide more conservative estimates of the fatigue limit.

	$\sqrt{area}$(μm)	$\Delta\sigma_{exp}$(MPa)	$\Delta\sigma_{th}$(MPa)	$\Delta\sigma_{SC}$(MPa)	$\frac{\Delta\sigma_{th}-\Delta\sigma_{exp}}{\Delta\sigma_{exp}}\bullet 100$	$\frac{\Delta\sigma_{SC}-\Delta\sigma_{exp}}{\Delta\sigma_{exp}}\bullet 100$
AB	62.0	130	102.0	93.7	−22	−28
HT1	72.6	120	112.3	92.7	−6	−23
HT2	84.5	100	99.0	98.2	−1	−2

4. Conclusions

This work provides an investigation of the influence of low temperature heat treatments on the fatigue behavior of a PBF-LB/M AlSi10Mg alloy. Fatigue specimens were produced in the form of vertical round bars on a build platform preheated at 200 °C. Some of the specimens were exposed to two different heat treatments: 265 °C for 1 h and 300 °C for 2 h. The round bars in as-built and heat-treated conditions were machined to the final shape of fatigue specimens. The defect population was determined by μCT scans, showing the presence of mainly spherical gas pores.

Unlike the fatigue crack propagation resistance results previously published by the authors in [22], no significant improvement of the fatigue performance has been observed after heat treatment. The whole fatigue data from the different material conditions fall well within a single scatter band. This is believed to depend on the size of the manufacturing defects, that are much larger than the microstructural features affected by the heat treatments (i.e., the disaggregation of the nanometric Si-network).

A better understanding of the fatigue data has been obtained by normalizing the applied stress range $\Delta\sigma$ by the threshold stress range $\Delta\sigma_{th}$ correspondent to the killer defect from which the failure originated. The fatigue data for HT1 and HT2, plotted in terms of $\Delta\sigma/\Delta\sigma_{th}-N$, showed a narrower scatter band. The AB specimens showed a superior fatigue strength, which is believed to be an indicator of the influence of microstructure on crack initiation.

The fatigue strength could be predicted well by different models, with short crack models (which consider the development of crack

closure with crack extension) providing the most conservative predictions. The equivalence to the method by Maierhofer et al. [48] and the resistance curve method proposed by Tanaka and Akiniwa [44] is demonstrated.

CRediT authorship contribution statement

Ilaria Roveda: Visualization, Methodology, Investigation, Formal analysis, Data curation, Conceptualization. **Itziar Serrano-Munoz:** Writing – review & editing, Writing – original draft, Visualization, Supervision, Project administration, Methodology, Investigation, Funding acquisition, Formal analysis, Conceptualization. **Jan Haubrich:** Writing – review & editing, Resources. **Guillermo Requena:** Writing – review & editing, Resources. **Mauro Madia:** Writing – review & editing, Writing – original draft, Visualization, Supervision, Project administration, Methodology, Investigation, Formal analysis, Conceptualization.

Declaration of competing interest

The authors declare that they have no known competing financial interests or personal relationships that could have appeared to influence the work reported in this paper.

Data availability

Data will be made available on request.

Acknowledgements

This work was supported by internal funding (MIT1-2019-40) at the Bundesanstalt für Materialforschung und –prüfung (BAM). Björn Mieller (Bundesanstalt für Materialforschung und -prüfung (BAM), Berlin, Germany) is acknowledged for performing the heat treatments.

References

[1] M. Armstrong, H. Mehrabi, N. Naveed, An overview of modern metal additive manufacturing technology, J. Manuf. Process. 84 (2022) 1001–1029, https://doi.org/10.1016/j.jmapro.2022.10.060.
[2] S. Pratheesh Kumar R. Naveen Anthuvan K. Anand S. Sanjith Raj P. m. Sachin Dhaman, et al., Technology overview of metal additive manufacturing processes Proceedings of the International Conference on Recent Advances in Manufacturing Engineering Research 2021 Icramer 2021, (2022), 10.1063/5.0095646.
[3] N.T. Aboulkhair, M. Simonelli, L. Parry, I. Ashcroft, C. Tuck, et al., 3D printing of Aluminium alloys: Additive Manufacturing of Aluminium alloys using selective laser melting, Prog. Mater Sci. 106 (2019), https://doi.org/10.1016/j.pmatsci.2019.100578.
[4] J. Zhang, B.o. Song, Q. Wei, D. Bourell, Y. Shi, A review of selective laser melting of aluminum alloys: Processing, microstructure, property and developing trends, J. Mater. Sci. Technol. 35 (2) (2019) 270–284, https://doi.org/10.1016/j.jmst.2018.09.004.
[5] A. Yadollahi, N. Shamsaei, Additive manufacturing of fatigue resistant materials: Challenges and opportunities, Int. J. Fatigue 98 (2017) 14–31, https://doi.org/10.1016/j.ijfatigue.2017.01.001.
[6] N. Limbasiya, A. Jain, H. Soni, V. Wankhede, G. Krolczyk, et al., A comprehensive review on the effect of process parameters and post-process treatments on microstructure and mechanical properties of selective laser melting of AlSi10Mg, J. Mater. Res. Technol. 21 (2022) 1141–1176, https://doi.org/10.1016/j.jmrt.2022.09.092.
[7] Z. Jiang, J. Sun, F. Berto, X. Wang, G. Qian, Fatigue and Fracture Behavior of AlSi10Mg Manufactured by Selective Laser Melting: A Review, Phys. Mesomech. 26 (4) (2023) 367–390, https://doi.org/10.1134/s102995992304001x.
[8] H. Liu, H. Yu, C. Guo, X. Chen, S. Zhong, et al., Review on Fatigue of Additive Manufactured Metallic Alloys: Microstructure, Performance, Enhancement and Assessment Methods e2306570 (2023), https://doi.org/10.1002/adma.202306570.
[9] C. Hutchinson, Resistance to fatigue, Nat Mater 22 (10) (2023) 1163–1164, https://doi.org/10.1038/s41563-023-01666-2.
[10] Ö. Karakaş, Feride Buket Kardeş, Pietro Foti, Filippo Berto, An overview of factors affecting high-cycle fatigue of additive manufacturing metals, Fatigue Fract. Eng. Mater. Struct. 46 (5) (2023) 1649–1668, https://doi.org/10.1111/ffe.13967.
[11] U. Zerbst, G. Bruno, J.-Y. Buffière, T. Wegener, T. Niendorf, et al., Damage tolerant design of additively manufactured metallic components subjected to cyclic loading: State of the art and challenges, Prog. Mater Sci. 121 (2021) 100786, https://doi.org/10.1016/j.pmatsci.2021.100786.
[12] W. Tang, Z. Tang, Lu. Wenjun, S. Wang, M. Yi, Modeling and Prediction of Fatigue Properties of Additively Manufactured Metals, Acta Mech. Solida Sin. 36 (2) (2023) 181–213, https://doi.org/10.1007/s10338-023-00380-5.
[13] Yves Nadot, Carole Nadot-Martin, Wen Hao Kan, Sarah Boufadene, Matthew Foley, et al., Predicting the fatigue life of an AlSi10Mg alloy manufactured via laser powder bed fusion by using data from computed tomography, *Additive Manufacturing*, (2020), *32,* 10.1016/j.addma.2019.100899.
[14] S. Afazov, A. Serjouei, G.J. Hickman, R. Mahal, D. Goy, et al., Defect-based fatigue model for additive manufacturing, Progress in Additive Manufacturing (2022), https://doi.org/10.1007/s40964-022-00376-6.
[15] S. Beretta, L. Patriarca, M. Gargourimotlagh, A. Hardaker, D. Brackett, et al., A benchmark activity on the fatigue life assessment of AlSi10Mg components manufactured by L-PBF, Mater. Des. 218 (2022), https://doi.org/10.1016/j.matdes.2022.110713.
[16] E. Brandl, U. Heckenberger, V. Holzinger, D. Buchbinder, Additive manufactured AlSi10Mg samples using Selective Laser Melting (SLM): Microstructure, high cycle fatigue, and fracture behavior, Mater. Des. 34 (2012) 159–169, https://doi.org/10.1016/j.matdes.2011.07.067.
[17] Julius N. Domfang Ngnekou, Yves Nadot, Gilbert Henaff, Julien Nicolai, Wen Hao Kan, et al., Fatigue properties of AlSi10Mg produced by Additive Layer Manufacturing, *International Journal of Fatigue*, (2019), *119,* 160-172, https://doi.org/10.1016/j.ijfatigue.2018.09.029.
[18] A. Kempf, J. Kruse, M. Madia, K. Hilgenberg, Correlation between quasistatic und fatigue properties of additively manufactured AlSi10Mg using Laser Powder Bed Fusion, Procedia Struct. Integrity 38 (2022) 77–83, https://doi.org/10.1016/j.prostr.2022.03.009.
[19] Iso, 6507–1:2018, Metallic materials — Vickers hardness test — Part 1, Test Method (2018). https://www.iso.org/standard/64065.html.
[20] A. Tridello, J. Fiocchi, C.A. Biffi, G. Chiandussi, M. Rossetto, et al., Influence of the annealing and defects on the VHCF behavior of an SLM AlSi10Mg alloy, Fatigue Fract. Eng. Mater. Struct. 42 (12) (2019) 2794–2807, https://doi.org/10.1111/ffe.13123.
[21] M.M.H. Tusher, A. Ince, A systematic review on high cycle and very high cycle fatigue behavior of laser powder bed fused (L-PBF) Al-Si alloys, Eng. Fail. Anal. 154 (2023), https://doi.org/10.1016/j.engfailanal.2023.107667.
[22] Ilaria Roveda, Itziar Serrano-Munoz, Jan Haubrich, Guillermo Requena, Mauro Madia, Influence of post-process heat treatments on the fatigue crack propagation behaviour of a PBF-LB/M AlSi10Mg alloy, *International Journal of Fatigue*, (2023), *175,* 10.1016/j.ijfatigue.2023.107808.
[23] I. Roveda, I. Serrano-Munoz, T. Mishurova, M. Madia, T. Pirling, et al., Influence of a 265 °C heat treatment on the residual stress state of a PBF-LB/M AlSi10Mg alloy, J Mater Sci 57 (2022) 22082–22098, https://doi.org/10.1007/s10853-022-07997-w.
[24] Silvia Marola, Silvia Bosia, Alessandro Veltro, Gianluca Fiore, Diego Manfredi, et al., Residual stresses in additively manufactured AlSi10Mg: Raman spectroscopy and X-ray diffraction analysis, *Materials & Design*, (2021), *202,* 10.1016/j.matdes.2021.109550.
[25] J.G.S. Macías, T. Douillard, L.v. Zhao, E. Maire, G. Pyka, et al., Influence on microstructure, strength and ductility of build platform temperature during laser powder bed fusion of AlSi10Mg, Acta Mater. 201 (2020) 231–243, https://doi.org/10.1016/j.actamat.2020.10.001.
[26] J. Fite, S.E. Prameela, J.A. Slotwinski, T.P. Weihs, Evolution of the microstructure and mechanical properties of additively manufactured AlSi10Mg during room temperature holds and low temperature aging, Addit. Manuf. 36 (2020), https://doi.org/10.1016/j.addma.2020.101429.
[27] J. Fiocchi, A. Tuissi, C.A. Biffi, Heat treatment of aluminium alloys produced by laser powder bed fusion: A review, Mater. Des. 204 (2021), https://doi.org/10.1016/j.matdes.2021.109651.
[28] I. Serrano-Munoz, I. Roveda, A. Kupsch, B.R. Müller, G. Bruno, Synchrotron X-ray refraction detects microstructure and porosity evolution during in-situ heat treatments, Mater. Sci. Eng. A 838 (2022), https://doi.org/10.1016/j.msea.2022.142732.
[29] ISO 1099:2017, Metallic materials — Fatigue testing — Axial force-controlled method, 2017 https://www.iso.org/standard/67847.html.
[30] Y. Murakami, Metal Fatigue: Effects of Small Defects and Nonmetallic Inclusions, Elsevier, 2002 https://shop.elsevier.com/books/metal-fatigue-effects-of-small-defects-and-nonmetallic-inclusions/murakami/978-0-12-813876-2.
[31] S. Romano, A. Brückner-Foit, A. Brandão, J. Gumpinger, T. Ghidini, et al., Fatigue properties of AlSi10Mg obtained by additive manufacturing: Defect-based modelling and prediction of fatigue strength, Eng. Fract. Mech. 187 (2018) 165–189, https://doi.org/10.1016/j.engfracmech.2017.11.002.
[32] S. Beretta, M. Gargourimotlagh, S. Foletti, A. du Plessis, M. Riccio, Fatigue strength assessment of "as built" AlSi10Mg manufactured by SLM with different build orientations, Int. J. Fatigue 139 (2020) 105737, https://doi.org/10.1016/j.ijfatigue.2020.105737.
[33] Volume-Graphics, VGSTUDIO MAX. 2019. . https://www.volumegraphics.com/en/products/vgsm.html.
[34] Wu. Zhengkai, Wu. Shengchuan, J. Bao, W. Qian, S. Karabal, et al., The effect of defect population on the anisotropic fatigue resistance of AlSi10Mg alloy fabricated by laser powder bed fusion, Int. J. Fatigue (2021) 151, https://doi.org/10.1016/j.ijfatigue.2021.106317.
[35] S. Romano, A. Brandão, J. Gumpinger, M. Gschweitl, S. Beretta, Qualification of AM parts: Extreme value statistics applied to tomographic measurements, Mater. Des. 131 (2017) 32–48, https://doi.org/10.1016/j.matdes.2017.05.091.
[36] S. Ghosh, S. Resnick, A discussion on mean excess plots, Stoch. Process. Appl. 120 (8) (2010) 1492–1517, https://doi.org/10.1016/j.spa.2010.04.002.

[37] H.P. Gänser, J. Maierhofer, T. Christiner, Statistical correction for reinserted runouts in fatigue testing, Int. J. Fatigue 80 (2015) 76–80, https://doi.org/10.1016/j.ijfatigue.2015.05.015.
[38] S. Beretta, M. Carboni, M. Madia, Modelling of fatigue thresholds for small cracks in a mild steel by "Strip-Yield" model, Eng. Fract. Mech. 76 (10) (2009) 1548–1561, https://doi.org/10.1016/j.engfracmech.2009.04.015.
[39] H. Kitagawa, Applicability of Fracture Mechanics to Very Small Cracks or the Cracks in the Early Stage, Proceedings of 2nd ICM, Cleveland, 627-631., 1976.
[40] M.H. El Haddad, K.N. Smith, T.H. Topper, Fatigue Crack Propagation of Short Cracks, J. Eng. Mater. Technol. 101 (1) (1979) 42–46, https://doi.org/10.1115/1.3443647.
[41] M.H. El Haddad, T.H. Topper, K.N. Smith, Prediction of non propagating cracks, Eng. Fract. Mech. 11 (3) (1979) 573–584, https://doi.org/10.1016/0013-7944(79)90081-X.
[42] S. Beretta, S. Romano, A comparison of fatigue strength sensitivity to defects for materials manufactured by AM or traditional processes, Int. J. Fatigue 94 (2017) 178–191, https://doi.org/10.1016/j.ijfatigue.2016.06.020.
[43] U. Zerbst, M. Madia, M. Vormwald, H. Th Beier, Fatigue strength and fracture mechanics – A general perspective, Eng. Fract. Mech. 198 (2018) 2–23, https://doi.org/10.1016/j.engfracmech.2017.04.030.
[44] K. Tanaka, Y. Akiniwa, Resistance-curve method for predicting propagation threshold of short fatigue cracks at notches, Eng. Fract. Mech. 30 (6) (1988) 863–876, https://doi.org/10.1016/0013-7944(88)90146-4.
[45] B. Tabernig, P. Powell, Reinhard Pippan, Resistance curves for the threshold of fatigue crack propagation in particle reinforced aluminum alloys, ASTM Spec. Tech. Publ. (2000) 96–108. https://www.astm.org/stp13428s.html.
[46] M. Chapetti, Fatigue propagation threshold of short cracks under constant amplitude loading, Int. J. Fatigue 25 (12) (2003) 1319–1326, https://doi.org/10.1016/s0142-1123(03)00065-3.
[47] J. Maierhofer, S. Kolitsch, R. Pippan, H.-P. Gänser, M. Madia, et al., The cyclic R-curve – Determination, problems, limitations and application, Eng. Fract. Mech. 198 (2018) 45–64, https://doi.org/10.1016/j.engfracmech.2017.09.032.
[48] J. Maierhofer, H.P. Gänser, R. Pippan, Modified Kitagawa-Takahashi diagram accounting for finite notch depths, Int. J. Fatigue 70 (2015) 503–509, https://doi.org/10.1016/j.ijfatigue.2014.07.007.
[49] F. Sausto, P.E. Carrion, N. Shamsaei, S. Beretta, Fatigue failure mechanisms for AlSi10Mg manufactured by L-PBF under axial and torsional loads: The role of defects and residual stresses, Int. J. Fatigue 162 (2022), https://doi.org/10.1016/j.ijfatigue.2022.106903.
[50] I. Roveda, T. Mishurova, A. Evans, A.N. Fitch, J. Haubrich, et al., Evolution of interphase stress over a crack propagation plane as a function of stress relief heat treatments in a PBF-LB/M AlSi10Mg alloy, Strain e12475 (2024), https://doi.org/10.1111/str.12475.
[51] Y. Murakami, T. Takagi, K. Wada, H. Matsunaga, Essential structure of S-N curve: Prediction of fatigue life and fatigue limit of defective materials and nature of scatter, Int. J. Fatigue (2021) 146, https://doi.org/10.1016/j.ijfatigue.2020.106138.
[52] W.W. Wits, E. Amsterdam, Fatigue prediction and life assessment method for metal laser powder bed fusion parts, CIRP Ann. 72 (1) (2023) 129–132, https://doi.org/10.1016/j.cirp.2023.03.011.
[53] F. Concli, R. Gerosa, D. Panzeri, L. Fraccaroli, High and low cycle fatigue properties of selective laser melted AISI 316L and AlSi10Mg, Int. J. Fatigue (2023) 177, https://doi.org/10.1016/j.ijfatigue.2023.107931.
[54] R. Min-Seok Baek, T.-H. Kreethi, Y. Sohn, K.-A. Lee, Influence of heat treatment on the high-cycle fatigue properties and fatigue damage mechanism of selective laser melted AlSi10Mg alloy, Mater. Sci. Eng. A (2021) 819, https://doi.org/10.1016/j.msea.2021.141486.
[55] C. Zhang, H. Zhu, H. Liao, Y. Cheng, Hu. Zhiheng, et al., Effect of heat treatments on fatigue property of selective laser melting AlSi10Mg, Int. J. Fatigue 116 (2018) 513–522, https://doi.org/10.1016/j.ijfatigue.2018.07.016.
[56] P. Van Cauwenbergh, V. Samaee, L. Thijs, J. Nejezchlebova, P. Sedlak, et al., Unravelling the multi-scale structure-property relationship of laser powder bed fusion processed and heat-treated AlSi10Mg, Sci Rep 11, (1) (2021) 6423, https://doi.org/10.1038/s41598-021-85047-2.
[57] E. Beevers, A.D. Brandão, J. Gumpinger, M. Gschweitl, C. Seyfert, et al., Fatigue properties and material characteristics of additively manufactured AlSi10Mg – Effect of the contour parameter on the microstructure, density, residual stress, roughness and mechanical properties, Int. J. Fatigue 117 (2018) 148–162, https://doi.org/10.1016/j.ijfatigue.2018.08.023.
[58] F. Bosio, C. Phutela, N. Ghisi, A. Alhammadi, N.T. Aboulkhair, Tuning the microstructure and mechanical properties of AlSi10Mg alloy via in-situ heat-treatments in laser powder bed fusion, Mater. Sci. Eng. A (2023) 879, https://doi.org/10.1016/j.msea.2023.145268.
[59] F. Sausto, C. Tezzele, S. Beretta, Analysis of Fatigue Strength of L-PBF AlSi10Mg with Different Surface Post-Processes: Effect of Residual Stresses, *Metals* 12, (6) (2022), https://doi.org/10.3390/met12060898.
[60] Naor Elad Uzan, Shlomo Ramati, Roni Shneck, Nachum Frage, Ori Yeheskel, On the effect of shot-peening on fatigue resistance of AlSi10Mg specimens fabricated by additive manufacturing using selective laser melting (AM-SLM), Addit. Manuf. 21 (2018) 458–464, https://doi.org/10.1016/j.addma.2018.03.030.
[61] S. Bagherifard, N. Beretta, S. Monti, M. Riccio, M. Bandini, et al., On the fatigue strength enhancement of additive manufactured AlSi10Mg parts by mechanical and thermal post-processing, Mater. Des. 145 (2018) 28–41, https://doi.org/10.1016/j.matdes.2018.02.055.
[62] M. Bonneric, C. Brugger, B. Tranchand, A. Castro Moreno, J. Lesseur, et al., Defect sensitivity in L-PBF AlSi7Mg0.6 alloy subjected to fatigue load: Effect of load ratio and torsion loading, Int. J. Fatigue (2024), https://doi.org/10.1016/j.ijfatigue.2024.108154.